




# Saturable absorption of few-layer WS<sub>2</sub> and WSe<sub>2</sub> at exciton resonance

SHUANG LIANG,<sup>1</sup> YUZE LU,<sup>1</sup> HAIMU LIU,<sup>1</sup> XIAOHE SHANG,<sup>1</sup>  
RONGGUANG DU,<sup>1</sup> JIAMIN JI,<sup>1</sup> YILING YU,<sup>1</sup>  
AND SHUNPING ZHANG<sup>1,2,\*</sup> 

<sup>1</sup>Key Laboratory of Artificial Micro- and Nano-Structures of Ministry of Education, School of Physics and Technology, Wuhan University, Wuhan 430072, China

<sup>2</sup>Wuhan Institute of Quantum Technology, Wuhan 430206, China

\*spzhang@whu.edu.cn

**Abstract:** Layered materials such as graphene and transition metal dichalcogenides (TMDs) are excellent candidates as saturable absorbers. However, the saturable absorption of few-layer TMDs is usually measured at the typical wavelengths of lasers, away from the exciton resonances. In this work, we study the saturable absorption effects in one, two, and three-layer WS<sub>2</sub> and WSe<sub>2</sub>, around the A-exciton resonance, using a tunable pulsed laser. Power-dependent reflectance contrast indicates that the saturation power density thresholds are around  $5.5 \times 10^6$  W/cm<sup>2</sup> ( $3.8 \times 10^6$  W/cm<sup>2</sup>) for monolayer WS<sub>2</sub> (WSe<sub>2</sub>), showing an order of magnitude reduction at the exciton peak. The saturation power density threshold increases with the number of layers. The analytical solution to the dynamics equation illustrates how the laser parameters influence the experimentally measured threshold, highlighting the importance of pulse duration in saturable absorption. This result reveals the effect of exciton decay and exciton-exciton interactions on the nonlinear optical properties of TMDs and benefits the design of TMD-based active optical devices.

© 2025 Optica Publishing Group under the terms of the [Optica Open Access Publishing Agreement](#)

## 1. Introduction

Atomically thin two-dimensional materials, including graphene and transition metal dichalcogenides (TMDs), etc., have attracted significant attention due to their exceptional optical and electronic properties [1–5], including their nonlinear optical (NLO) effects [6]. The use of graphene as a saturable absorber is demonstrated as early as 2009 [7]. Known for its low saturation intensity, ultrafast recovery time, and broad tunability, graphene shows promise in applications like mode-locking in fiber lasers [8–14], active control of photonic devices [15–17]. Following this trajectory, the study of nonlinear optics in other layered 2D materials has gained traction over the past decade [18,19]. For example, the saturable absorption (SA) effects in MoS<sub>2</sub> nanosheets were reported in 2013 [20] and subsequent experiments reveal that few-layer TMDs, such as MoS<sub>2</sub> [21–26], MoSe<sub>2</sub> [23,25,27], WS<sub>2</sub> [21,24,25,28,29], and WSe<sub>2</sub> [21,25,30], offer superior saturable absorption compared to graphene under similar conditions.

Typically, SA and two-photon absorption responses were reported using z-scan measurements [20–24,30]. However, different studies used different experimental setups, laser parameters, and sample preparation methods (e.g., mechanical exfoliation, liquid-phase exfoliation, and chemical vapor deposition), making it less straightforward to compare the NLO behaviors across different TMDs. More importantly, most reports have focused on z-scan measurements at typical laser wavelengths (800 nm, 632.8 nm, 520 nm, 1550 nm, etc.) [20,24,31–33], leaving SA or two-photon absorption at wavelengths near the exciton resonances largely unexplored. Apart from studies utilizing monochromatic lasers, transient absorption spectroscopy using broadband probe light has also been employed to investigate the broad spectral response of TMDs beyond specific wavelengths of typical lasers, uncovering exciton dynamics [34–37] and various NLO

responses like bleaching, shifting, and photoinduced bandgap renormalization within the range of A exciton resonance [34,36,38–40]. These experimental findings have been further elucidated through theoretical models, considering phase-space filling and Coulomb screening effects, particularly in explaining the bleaching effect at exciton resonant peaks under high-power laser exposure [41–43]. Despite the use of a broadband probe light, transient absorption typically uses a pump beam with a specific wavelength. The saturable absorption at exciton resonant wavelengths, which characterizes the power-dependent NLO response of excitons, including the dynamics of exciton generation, dephasing, and exciton-exciton interaction, remains unexplored.

In this study, we conduct a comprehensive analysis of SA in few-layer WS<sub>2</sub> and WSe<sub>2</sub>, around the A exciton resonance, using a pulsed supercontinuum laser. By scanning the pumping wavelengths near the A exciton, we demonstrate the evolution of the saturation power density for different excitation wavelengths, material types, and number of layers. Notably, both WS<sub>2</sub> and WSe<sub>2</sub> showed significant decreases in reflectance contrast at the A exciton resonance, as the pump power densities increased, indicative of a strong saturable absorption behavior in few-layer TMDs. We observed that the saturation power density threshold for both materials lies between  $5.5 \times 10^6 \text{ W/cm}^2$  –  $2.12 \times 10^7 \text{ W/cm}^2$ , marking an order of magnitude reduction at the exciton peak. Furthermore, the saturation power density is found to increase with the number of layers. Through analytical solutions of the exciton dynamics equation, we investigate the ultrafast behavior exciton density under varying pulse durations, highlighting the critical influence of pulse duration on the saturation threshold and the NLO properties of materials. This result reveals the properties of exciton-exciton interaction in TMDs and benefits the design of TMD-based nonlinear optic devices.

## 2. Results and discussion

To characterize the SA of few-layer TMDs, we perform power-dependent reflectance contrast measurement under ambient conditions (Fig. 1(a)). First, the steady reflectance contrast of the samples was obtained using a halogen lamp source. The resonant position of the A exciton was identified by analyzing the broad-spectrum reflectance contrast response of the materials. Then, a supercontinuum laser source (NKT Photonics SuperK Extreme) in conjunction with acousto-optic tunable filters (AOTF) was used to select the wavelength around the A exciton with an FWHM of approximately 3 nm. The repetition rate and pulse duration of the laser source are 8.861 MHz and 78 ps, respectively. The peak power density of our pulsed laser is in the range of  $\sim 10^4 \text{ W/cm}^2$  –  $10^7 \text{ W/cm}^2$ , significantly below the laser peak power density damage thresholds of the optical lens and that of few-layer TMDs ( $0.5 \text{ GW/cm}^2$  –  $1 \text{ GW/cm}^2$ ) [21,44]. Since the laser is linearly polarized, the pumping power can be precisely adjusted by combining a polarizer and a half-wave plate mounted on a motorized rotational motor (Thorlabs PRM1Z8), without introducing distortion to the beam profile. Real-time power was monitored by splitting a portion of the laser beam into a power meter using a quartz plate. The sample, placed on a piezo stage (Thorlabs MAX313D), was moved into or outside the focus laser spot to repeat the reflection measurements 20 times. The measurement spanning a wide range of power levels and wavelengths, was implemented by a homemade control program that sequentially tuned the angle of the half-wave plate with respect to a polarizer and the wavelength selection of the AOTF. The spot size on the sample was focused to a diameter close to the diffraction limit using an objective lens (Olympus NA = 0.8, 100 ×). The reflected light was collected by the same objective and deflected by a beam splitter to a spectrometer equipped with a CCD camera (HORIBA iHR 550).

Figure 1(b) schematically illustrates the generation of exciton complexes with the increasing pump intensity. In the regime of low power density excitation, the optical properties of the TMDs are dominated by the exciton. As the pump power density increases, the interaction between excitons increases, and new quasi-particles such as trion, biexciton, etc. emerge [34]. SA appears due to the phase-space filling effect originating from the Pauli blocking. If the power density

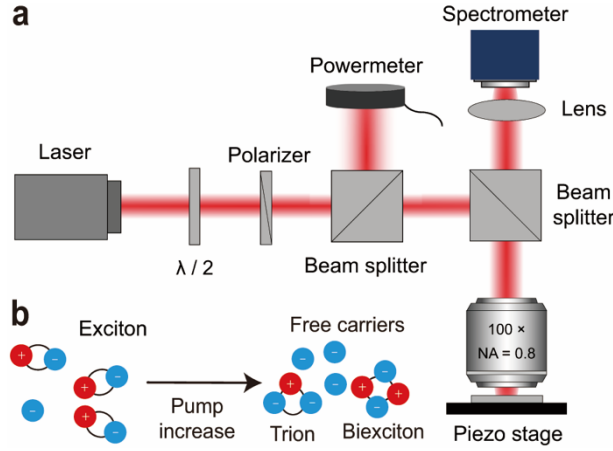


**Fig. 1.** (a) The schematic of the experimental setup. (b) Schematic of the generation of free carriers, exciton, trion, biexciton, etc., when the pump power increases.

goes even higher, a phase transition to plasma state or exciton liquid comes up such that the NLO response becomes significant.

Few-layer TMD samples are mechanically exfoliated from bulk crystals (HQ graphene) by scotch tape [45] and are transferred by PDMS stamp [46] onto quartz substrates. The thickness of atomic thin layers was first identified by their optical contrast under a microscope with verification by atomic force microscope (not shown), PL intensity, and Raman spectroscopy after all the optical measurements. PL and Raman spectra are shown in Fig. 2 with the excitation wavelength of 532 nm. Strong emission is observed at the energy corresponding to A excitonic resonance, which is  $\sim 612$  nm and  $\sim 747$  nm for 1 L  $\text{WS}_2$  and  $\text{WSe}_2$ , respectively. For  $\text{WS}_2$ , as the layer number increases to 2 L and 3 L, the A exciton emission peak decreases by approximately an order of magnitude compared to the 1 L sample, consistent with previous work [47]. Photoluminescence corresponding to indirect transition appears in the 2 L and 3 L samples at  $\sim 715$  nm and  $\sim 790$  nm, respectively, which is also consistent with previous reports [48]. Similarly, the A exciton emission peak similarly reduces significantly when increasing the layer number of  $\text{WSe}_2$  from 1 L to 3 L. Indirect luminescence is observed at  $\sim 800$  nm in 2 L samples and  $\sim 845$  nm in 3 L samples, also consistent with previous reports [48]. Figure 2(c) and 2(d) show the major Raman peaks of the samples, consistent with previous measurements [47,48]. For  $\text{WS}_2$ , the in-plane vibrational  $E_{2g}^1$  mode is redshift from  $\sim 354$   $\text{cm}^{-1}$  for 1 L to  $\sim 350$   $\text{cm}^{-1}$  for 3 L, while the out-of-plane  $A_{1g}$  mode is at  $\sim 418$   $\text{cm}^{-1}$ . For  $\text{WSe}_2$ , the  $E_{2g}^1$  mode is at  $\sim 250$   $\text{cm}^{-1}$  and the  $A_{1g}$  mode is at  $\sim 260$   $\text{cm}^{-1}$ . These consistency with previous measurements further confirms the quality of the exfoliated sample and the identification of the layer number.

At the wavelengths around A exciton, the absorption coefficient is significantly increased. Figures 3(a)-(c) illustrate the broadband reflectance contrast measurements for 1-layer (1 L), 2-layer (2 L), and 3-layer (3 L)  $\text{WS}_2$ . When increasing the layer number, a slight red-shift of the A exciton peak is observed in the reflectance contrast measurement. This shift is attributed to the narrowing of the bandgap energy when transitioning from monolayer TMDs to multilayer TMDs, consistent with previous reports [48]. The relation between the reflectance contrast  $\Delta R/R$  and the absorption coefficient  $\alpha_0$  is described by the following equations [49] (Supplement 1 S2):

$$\alpha_0 = \left| \frac{n_0 - 1}{n_0 + 1} \right| \Delta R/R, \quad (1)$$

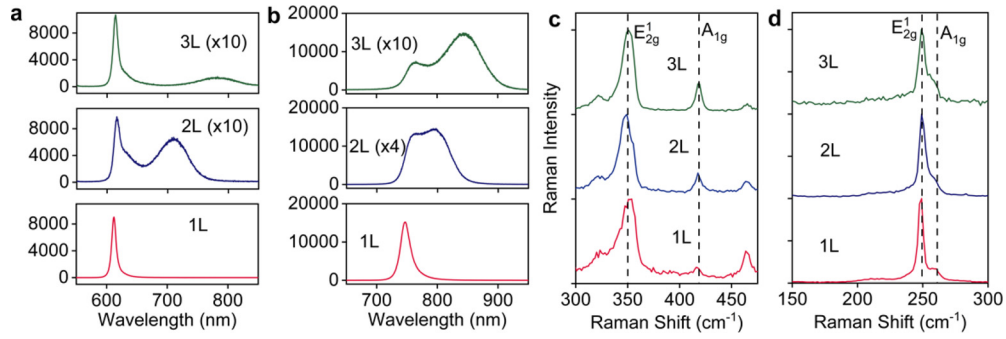


**Fig. 2.** (a, b) PL intensity of 1 L (red), 2 L (blue), and 3 L (green) WS<sub>2</sub> (a) and WSe<sub>2</sub> (b) samples. The curves are offset for clarity. (c, d) Raman spectra of 1 L (red), 2 L (blue), and 3 L (green) WS<sub>2</sub> (c) and WSe<sub>2</sub> (d) samples.

where  $n_0$  refers to the refractive index of the substrate and it is 1.46 for quartz in our study. Reflection contrast  $\Delta R/R$  is around 0.56 (1 L), 0.70 (2 L), and 1.13 (3 L) at the exciton resonance.

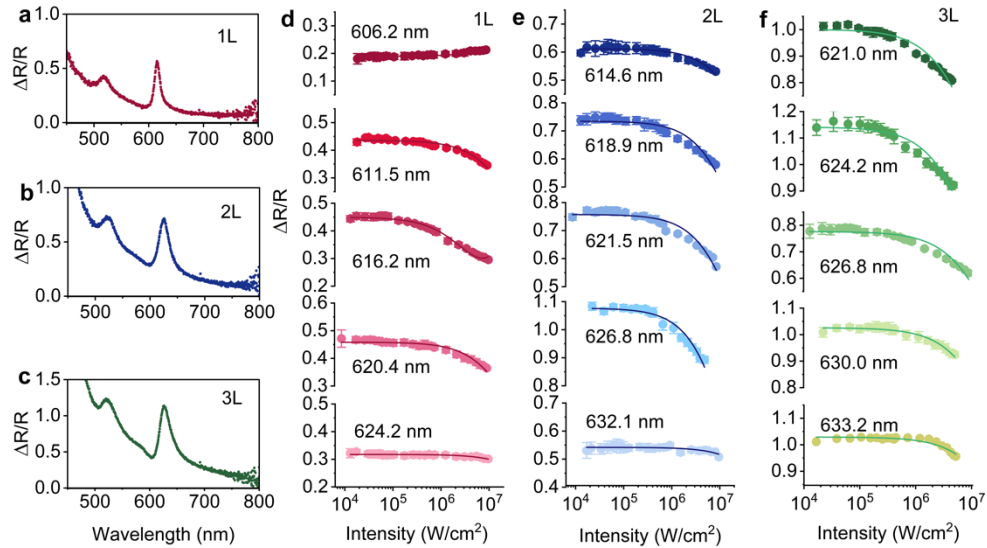


**Fig. 3.** Steady (a-c) and power-dependent pulsed (d-f) reflectance contrast of 1 L, 2 L, and 3 L WS<sub>2</sub> around A exciton resonance. The pumping wavelength is scanned across the exciton resonance. The curves for different pumping wavelengths are vertically shifted for clarity.

To study the power dependency of reflectance contrast of WS<sub>2</sub>, we chose five wavelengths across the A exciton peak, with a step of approximately 3 nm, centered at the wavelength of 616.2 nm, 621.5 nm and 624.2 nm, for 1 L, 2 L and 3 L WS<sub>2</sub>. The results are demonstrated in Fig. 3(d-f). At the peak wavelength (616.2 nm) of the A exciton,  $\Delta R/R$  is  $\sim 0.45$  in the low power density range, close to the value of steady reflectance contrast. As the peak power density increases to around  $9.8 \times 10^6$  W/cm<sup>2</sup>,  $\Delta R/R$  decreases to 0.29. On either the red or blue side of the A exciton, the reduction in reflectance contrast is less pronounced within the power density range of our measurements. For example, it decreases from 0.42 to 0.33 for 611.5 nm and from 0.46 to 0.38 for 620.4 nm, respectively. Notably, at 606.2 nm, the change in  $\Delta R/R$

increases as the pump power intensity rises, indicating the occurrence of two-photon absorption. At the resonant wavelength of A exciton in 2 L and 3 L samples,  $\Delta R/R$  is approximately 0.71 and 1.11, respectively, in the low power density range, which is also close to the steady reflectance contrast. As the pump wavelength shifts away from the resonant peak, the reduction of  $\Delta R/R$  in the power-dependent measurements also becomes less pronounced.

Figures 4(a)-(c) illustrate the broadband reflectance contrast measurements for 1 L, 2 L, and 3 L WSe<sub>2</sub>. Normalized reflection contrast  $\Delta R/R$  is around 0.48 (1 L), 0.58 (2 L), and 0.91 (3 L) at the exciton resonance. Figure 4(d)-(f) presents the result of power-dependent measurement for 1 L, 2 L, and 3 L WSe<sub>2</sub> samples, at the five wavelengths selected across the A exciton peak. For 1 L WSe<sub>2</sub> at the peak wavelength of A exciton,  $\Delta R/R$  is around 0.47 in the low power density range, close to the value of steady reflectance contrast. As the peak power density increases to around  $9.6 \times 10^6$  W/cm<sup>2</sup>,  $\Delta R/R$  decreases to  $\sim 0.28$ . When the pump wavelength is shifted to the red or blue side of A exciton, the reduction of reflectance contrast becomes smaller. It decreases from 0.46 to 0.30 at 743 nm and from 0.41 to 0.3 at 749.3 nm. For 2 L and 3 L WSe<sub>2</sub>,  $\Delta R/R$  is around 0.66 and 0.86 at the peak wavelength of A exciton in the low power density range. As the pump wavelength shifts away from the resonant peak, the reduction of  $\Delta R/R$  in the power-dependent measurements also becomes less pronounced, similar to the case in WS<sub>2</sub>.

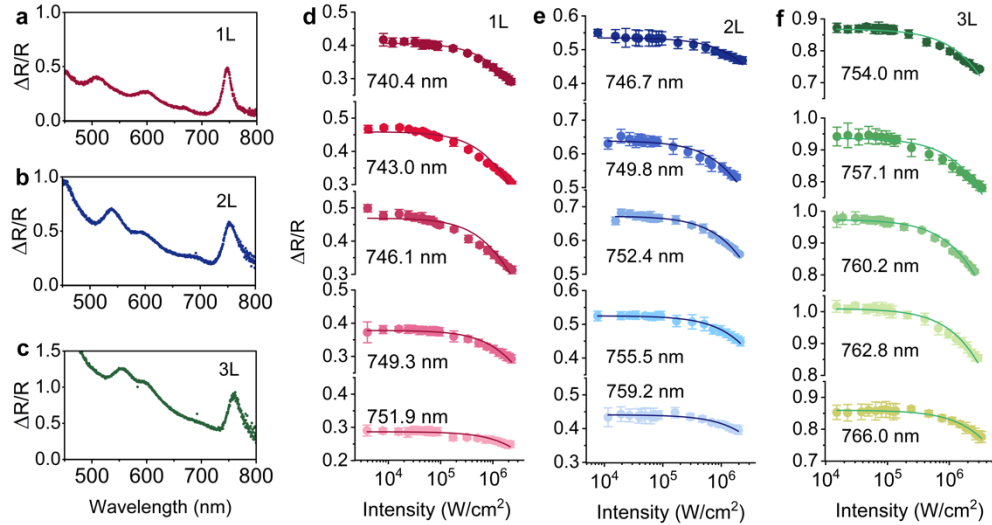


**Fig. 4. Steady (a-c) and power-dependent pulsed (d-f) reflectance contrast of 1 L, 2 L, and 3 L WSe<sub>2</sub> around A exciton resonance.** The pumping wavelength is scanned across the exciton resonance. The curves for different pumping wavelengths are vertically shifted for clarity.

To exclude artifacts from the experiment setup, we repeat the experiments far from the exciton resonance, as shown in Supplement 1 Figs. S8-S9. No significant decrease in the reflectance contrast was observed at these wavelengths within the power density range of our measurements. Therefore, we can attribute the decreases in reflectance contrast to the Pauli blocking effect at the exciton resonance. As the power density increases, the presence of exciton prevents further optical transitions, meaning that the A exciton is bleached. In high-density regimes, exciton-exciton scattering can also be included to explain the decrease in the absorption peak [41]. To extract the threshold intensity of SA and the coefficient of two-photon absorption, we can fit the measured absorption coefficient  $\alpha$  according to the following equation [20]

$$\alpha(I) = \frac{\alpha_0}{1 + I/I_s} + \beta I, \quad (2)$$



where  $I$  is the pump power density,  $\beta$  is the coefficient of two-photon absorption and  $I_s$  is the saturation power density threshold at which the absorption coefficient  $\alpha$  is reduced to half of its original value  $\alpha_0$ . By fitting the measured reflectance contrast at different pump intensities to Eq. (2), the saturation threshold intensity can be obtained, as shown by the solid lines in Fig. 3(d)-(f) and Fig. 4(d)-(f). At the peak wavelength of the A exciton, the saturation threshold intensity is  $5.5 \times 10^6$ ,  $2.4 \times 10^7$  and  $2.1 \times 10^7$  W/cm<sup>2</sup> for 1 L, 2 L and 3 L WS<sub>2</sub>, and  $3.8 \times 10^6$ ,  $8.0 \times 10^6$  and  $1.2 \times 10^7$  W/cm<sup>2</sup>, for 1 L, 2 L and 3 L WSe<sub>2</sub>, respectively. Obviously, the saturation threshold intensity increases with the number of layers. Note that in the fittings, we intentionally set the coefficient of two-photon absorption to zero to obtain the best fit, except at the wavelength of 616.2 nm and 606.2 nm for the 1 L WS<sub>2</sub> sample. At these specific wavelengths, the influence of two-photon absorption can partially offset the effect of SA and therefore cannot be neglected in the fitting.

To understand the evolution of the saturation threshold  $I_s$  around the A-exciton peak, we plot the power density threshold for both WS<sub>2</sub> and WSe<sub>2</sub> in Fig. 5. Consistently across all samples, the lowest power density threshold occurs at the wavelength corresponding to the A-exciton resonant peak. For samples with the same layer number, WS<sub>2</sub> exhibits a higher threshold power density than WSe<sub>2</sub>. No clear signs of two-photon absorption are observed in the WSe<sub>2</sub> samples in the experimental range of pumping power density, while the appearance of two-photon absorption is clear in the 1 L WS<sub>2</sub> sample.

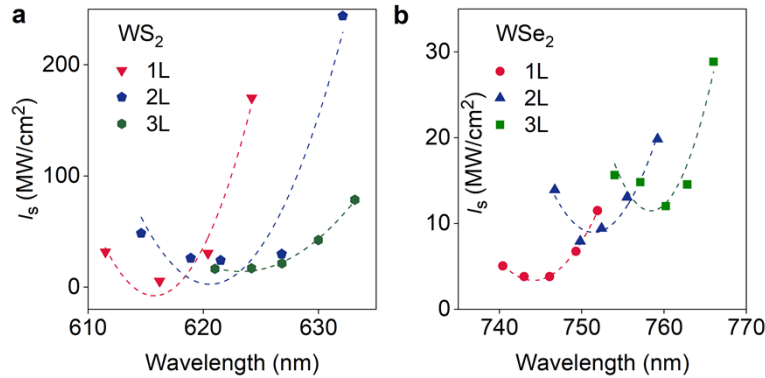


**Fig. 5. Comparison of the saturation threshold for few-layer WS<sub>2</sub> and WSe<sub>2</sub>.** (a) Threshold comparison of few-layer WS<sub>2</sub>. (b) Threshold comparison of few-layer WSe<sub>2</sub>.

For both WS<sub>2</sub> and WSe<sub>2</sub> samples, the saturation power density threshold increases as the layer number increases. For an incident light of a given power density, the exciton density in thicker layers is lower than that in thinner layers, though the absorption coefficient is higher for thicker layers. For example, comparing the 1 L and 2 L WS<sub>2</sub>, the volume and so the total number of atoms (the total electronic states are proportional to this number) is different by two times, but the difference in the steady absorption coefficient is obviously smaller, 0.106 vs 0.134, according to Fig. 3(a) and Eq. (3). Consequently, the multilayer structure is less prone to saturation.

Previous research has demonstrated the layer-dependent saturation threshold for WS<sub>2</sub> at the wavelength of 800 nm, indicating that the saturation threshold decreases with layer number [33]. As shown in Fig. 3(a)–3(c), this change in the saturation threshold is mainly due to the redshift of the exciton resonant wavelength as the layer number increases, approaching the pumping light. According to Fig. 5, the saturation threshold would decrease as the exciton resonant wavelength approaches the pump wavelength, or alternatively, the exciton resonance dominates the NLO saturation behaviors. Comparing the WS<sub>2</sub> and WSe<sub>2</sub>, the variance of the saturation threshold of WS<sub>2</sub> is more sensitive to the deviation from the A-exciton resonant peak than that

of WSe<sub>2</sub>, because the exciton resonance is stronger for WS<sub>2</sub>. Compared with previous works using non-resonant excitation, resonant excitation has about two orders of magnitude lower in saturation power density threshold.

### 3. Theoretical analysis

A comparison between the saturation intensity and corresponding exciton density in our experiments and previous works is summarized in Table 1. It shows that the saturation intensity varies for different materials, pump wavelengths pulse duration, etc. In this section, we propose a theoretical model to further elucidate the dependence of the saturation power density threshold on the pulse duration.

**Table 1. Comparison of the saturation threshold of few layer TMDs**

Sample	Pump wavelength (Repetition Rate, Pulse Duration)	$I_s$ (W/cm <sup>2</sup> )	$n_s$ (cm <sup>-2</sup> )	Reference
WS <sub>2</sub>	1550 nm (37 MHz, 560 fs)	$1.48 \times 10^8$	NA	[24]
WSe <sub>2</sub>	1550 nm (37 MHz, 560 fs)	$2.7 \times 10^8$	NA	[24]
MoS <sub>2</sub> /CHP	800 nm (1 kHz, 100 fs)	$4.05 \times 10^{11}$	NA	[20]
21 L WS <sub>2</sub>	800 nm (1 kHz, 35 fs)	$2.08 \times 10^{11}$	NA	[33]
22 L MoS <sub>2</sub>	800 nm (1 kHz, 35 fs)	$5.52 \times 10^{11}$	NA	[33]
1 L WS <sub>2</sub>	803 nm (91 MHz, 15ps)	$6.86 \times 10^4$	NA	[50]
1 L MoS <sub>2</sub>	520 nm (1 kHz, 350 fs)	NA	$4.1 \times 10^{12}$	[32]
1 L MoSe <sub>2</sub>	520 nm (1 kHz, 350 fs)	NA	$6.9 \times 10^{12}$	[32]
1 L WS <sub>2</sub>	520 nm (1 kHz, 350 fs)	NA	$3.29 \times 10^{12}$	[32]
1 L WSe <sub>2</sub>	520 nm (1 kHz, 350 fs)	NA	$3.83 \times 10^{12}$	[32]
1 L WS <sub>2</sub>	616.2 nm (8.66 MHz, 78 ps)	$5.5 \times 10^6$	$1.1 \times 10^{13}$	This work
2 L WS <sub>2</sub>	621.5 nm (8.66 MHz, 78 ps)	$2.4 \times 10^7$	NA	This work
3 L WS <sub>2</sub>	624.2 nm (8.66 MHz, 78 ps)	$2.1 \times 10^7$	NA	This work
1 L WSe <sub>2</sub>	743.0 nm (8.66 MHz, 78 ps)	$3.8 \times 10^6$	$6.9 \times 10^{12}$	This work
2 L WSe <sub>2</sub>	749.8 nm (8.66 MHz, 78 ps)	$8.0 \times 10^6$	NA	This work
3 L WSe <sub>2</sub>	760.2 nm (8.66 MHz, 78 ps)	$1.2 \times 10^7$	NA	This work

After light absorption, the exciton density  $n$  is generally determined by [34]:

$$n = \frac{I\tau\alpha}{N\hbar\nu}\eta, \quad (3)$$

where  $\tau$  is the lifetime of the exciton,  $\alpha$  is the absorption coefficient of TMDs,  $N$  is the number of layers,  $\hbar\nu$  is the photon energy of the pump light, and  $\eta$  is the efficiency of generating an exciton when absorbing a single photon, which is close to unity for resonant excitation. As an initial analysis for Eq. (2), the saturation threshold  $I_s$ , at which the absorption coefficient drops to one-half, corresponds to a saturation exciton density  $n_s$  that is half of the total exciton states available for absorption. Since the total available absorption state is a constant over a certain frequency region, for a given material, the saturation threshold will follow  $I_s(\lambda) \sim \alpha^{-1}(\lambda)$ . This implies a dip at the exciton resonance if  $\eta$  does not vary significantly over the small spectral range used. This qualitatively explains the reduction of saturation threshold at the exciton peak shown in Fig. 5(b). For different layer numbers, though the total absorption increases as the layer number  $N$  increases, the volume (thickness) of the layer increases as well. Then, the exciton density decreases considering that the absorption coefficient per unit length  $\alpha/N$  decreases for 2 L or 3 L samples, compared with the monolayer. Therefore, the saturation threshold at exciton resonance increases as the number of layers. Previous studies by z-scan measurement using 100

fs pulses show a clear SA at 800 nm for MoS<sub>2</sub> from liquid-phase exfoliation [20]. The bleaching effect was also reported in broadband pump-probe measurement, where the reduction of the resonant peak in reflectance contrast is remarkable at high pump intensity [36,41].

To disentangle the contribution of wavelength and pulse duration to the saturation threshold intensity, we solve the empirical dynamics equation of carriers using a pulse excitation. Since the exciton-exciton annihilation effect can be strong at high power densities [32,51,52], the exciton dynamics equation including the exciton-exciton annihilation effect could be written as

$$\frac{dn}{dt} = G - \frac{n}{\tau} - \gamma n^2, \quad (4)$$

where  $G = I\alpha_0\lambda/hc(1 + I/I_s)$  is the generation rate of exciton,  $\gamma$  is the annihilation rate from the exciton-exciton interaction [32]. Considering the pump laser pulse as a square function with a pulse duration  $\tau_p$ , it follows

$$I(t) = \begin{cases} I_0, & 0 \leq t \leq \tau_p \\ 0, & t > \tau_p \end{cases} \quad (5)$$

The analytical solution for Eq. (4) under the condition of Eq. (5) could be written as follows:

$$n(t) = \begin{cases} \frac{m_0 e^{2B\gamma t} + 1}{m_0 e^{2B\gamma t} - 1} \sqrt{\frac{G}{\gamma} + \frac{1}{4\gamma^2\tau^2}} - \frac{1}{2\gamma\tau}, & 0 \leq t \leq \tau_p \\ \left( \frac{2}{q_0 e^{2B\gamma t} - 1} \right) \frac{1}{2\gamma\tau}, & t > \tau_p \end{cases}, \quad (6)$$

where  $m_0$  and  $q_0$  are constants determined by the initial exciton density and  $B$  is defined as:

$$B = \sqrt{\frac{G}{\gamma} + \frac{1}{4\gamma^2\tau^2}} \quad (7)$$

Equations (6)–(7) describe the dynamics under single pulse excitation. It applies to those cases where the pulse separation, i.e., the reciprocal of the repetition rate of the laser, is much larger than the characteristic time scale of the exciton. If the repetition rate of the laser is high, the analytical solution of Eq. (4) under periodic excitation could be written as

$$n(t) = \begin{cases} \frac{m_k e^{2B\gamma t} + 1}{m_k e^{2B\gamma t} - 1} \sqrt{\frac{G}{\gamma} + \frac{1}{4\gamma^2\tau^2}} - \frac{1}{2\gamma\tau}, & kT \leq t \leq kT + \tau_p \\ \left( \frac{q_k e^{2B\gamma t} + 1}{q_k e^{2B\gamma t} - 1} - 1 \right) \frac{1}{2\gamma\tau}, & kT + \tau_p < t < kT + T \end{cases}, \quad (8)$$

where  $q_k$  and  $m_{k+1}$  are undetermined coefficients for period  $k$  and  $k+1$ . These coefficients could be derived from the recursive relations according to the boundary conditions introduced by the consistency of exciton density:

$$\left( \frac{q_k e^{2B\gamma(kT+\tau_p)} + 1}{q_k e^{2B\gamma(kT+\tau_p)} - 1} - 1 \right) \frac{1}{2\gamma\tau} = \frac{m_k e^{2B\gamma(kT+\tau_p)} + 1}{m_k e^{2B\gamma(kT+\tau_p)} - 1} \sqrt{\frac{G}{\gamma} + \frac{1}{4\gamma^2\tau^2}} - \frac{1}{2\gamma\tau}, \quad (9)$$

$$\left( \frac{q_k e^{2B\gamma(k+1)T} + 1}{q_k e^{2B\gamma(k+1)T} - 1} - 1 \right) \frac{1}{2\gamma\tau} = \frac{m_{k+1} e^{2B\gamma(k+1)T} + 1}{m_{k+1} e^{2B\gamma(k+1)T} - 1} \sqrt{\frac{G}{\gamma} + \frac{1}{4\gamma^2\tau^2}} - \frac{1}{2\gamma\tau}. \quad (10)$$

Figure 6(a) demonstrates the dynamics of transient exciton density under different pulse duration in 1 L WS<sub>2</sub> according to Eqs. (8)–(10). The laser repetition rate is set to 8.66 MHz, consistent with our experimental parameters, and the pump intensities are 5.5 MW/cm<sup>2</sup> for WS<sub>2</sub> and 3.8 MW/cm<sup>2</sup> for WSe<sub>2</sub>, respectively. The lifetime of the exciton  $\tau$  and the annihilation rate



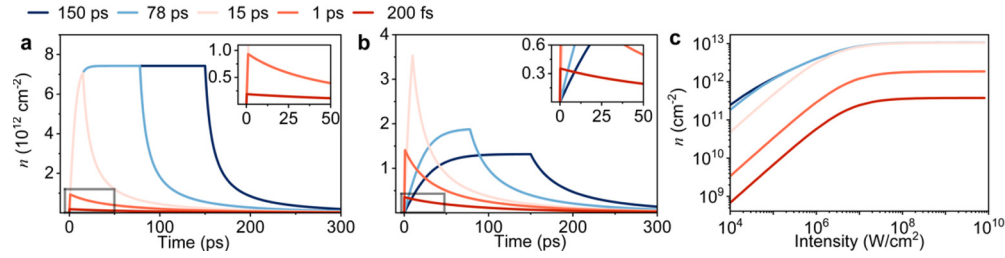


**Fig. 6.** The evolution of exciton density in monolayer WS<sub>2</sub> for different pulse durations. (a) Transient dynamics of exciton density under constant pump intensity. (b) Transient dynamics of exciton density under constant single pulse energy (17.16 μJ/cm<sup>2</sup>). The insets in (a, b) shows an enlarged view of the gray box. (c) The evolution of peak exciton density under various pump fluences. The threshold intensity  $I_s$  is assumed to be  $5.5 \times 10^6$  W/cm<sup>2</sup> corresponding to 1 L WS<sub>2</sub>.

from the exciton-exciton interaction  $\gamma$  of WS<sub>2</sub> and WSe<sub>2</sub> ( $\tau = 124.665$  ps,  $\gamma = 0.016$  cm<sup>2</sup>/s for 1 L WS<sub>2</sub>;  $\tau = 115.8$  ps,  $\gamma = 0.026$  cm<sup>2</sup>/s for 1 L WSe<sub>2</sub>) are taken from Ref. [32]. Based on these parameters, the estimated saturation exciton densities are  $1.1 \times 10^{13}$  cm<sup>-2</sup> for 1 L WS<sub>2</sub> and  $6.9 \times 10^{12}$  cm<sup>-2</sup> for 1 L WSe<sub>2</sub>.

For larger pulse durations, the exciton density does not increase over the entire pulse duration but saturates because of the strong exciton-exciton annihilation process at high exciton densities. From the curves, the characteristic rising (decay) time of the exciton density can be determined to be 5.49 ps (13.5 ps), corresponding mostly to the exciton-exciton interaction strength. For very short pulses, the total energy per pulse is insufficient to pump the sample to reach the threshold exciton density. In this case, the nonlinearity from the materials will be much weaker even though the peak intensity of the pump has reached the threshold intensity.

Figure 6(b) illustrates the influence of the pulse duration on the transient exciton density in 1 L WS<sub>2</sub> under constant single pulse energy. Shorter pulses have higher peak power density compared to longer pulses, enabling a higher exciton generation rate and making it easier to reach the saturation exciton density threshold. However, the pulse duration must also align with the characteristic timescale of the material, specifically the rising time of exciton density (5.49 ps for 1 L WS<sub>2</sub>, as determined earlier). For pulse durations much shorter than this characteristic rising time, the peak exciton density decreases significantly because the material cannot absorb sufficient light before the excitons are annihilated. In contrast, for pulse durations longer than the characteristic rising time, shorter pulses result in a larger peak exciton density. This is due to the dynamic balance between exciton creation via light absorption and exciton annihilation during longer pulses, which limits the peak exciton density.

This analysis also explains the observed differences between our measured saturation peak power density using a picosecond pulsed laser and previous measurements with femtosecond lasers [24,32,33,50]. The significantly shorter pulse durations in femtosecond experiments fall well below the characteristic rising time of exciton density. Consequently, higher pump intensities are required to compensate for the insufficient pulse duration, resulting in a higher observed saturation peak power density in those experiments.

We can also calculate the peak exciton density for monolayer WS<sub>2</sub> as a function of peak pump intensity for different pulse durations, as shown in Fig. 6(c). It is clear that the exciton density can always reach a maximum under different pulse durations. But only when the pulse duration is large enough compared with the characteristic time scale of the material can the maximum approach its limit. As depicted in Fig. 6(c), the estimated saturation exciton density for 1 L WS<sub>2</sub> reaches approximately  $10^{12}$  cm<sup>-2</sup> under the pulse duration of 78 ps, consistent with thresholds reported in Ref. [32]. The material saturates at a lower exciton density yet higher

pump intensity under shorter pulse durations. As the pulse duration increases, the saturation exciton density saturates at a certain level as a result of the strong exciton-exciton annihilation effect. The extended discussion here aims to explain that with longer pulse durations, the high exciton density state occupies a longer transient scale, hence more easily reaching saturation. Simultaneously, while the peak exciton density increases with pulse width, this increase is not unbounded due to the impracticality of excessively high exciton densities, which would surpass the Mott transition threshold.

Figure 6 also implies guidelines for the choice of laser parameters in measuring the saturation threshold, especially the pulse duration. If the single pulse energy is significantly large, a longer pulse duration is better to observe the nonlinearity of the material. On the contrary, very short pulses lead to unbleached samples because of the slow accumulation of the exciton density. If single pulse energy is limited to a low level, one should choose a shorter pulse to reach the threshold intensity of the material. A preferred option is pulse duration comparable to the characteristic time scale of the exciton, then the peak exciton density can reach as high as possible for a limited single pulse energy.

#### 4. Conclusion

In summary, we carried power-dependent measurements on 1~3 layer WS<sub>2</sub> and WSe<sub>2</sub>, extracting the saturation threshold as a function of pumping wavelength. For both WS<sub>2</sub> and WSe<sub>2</sub>, the power density threshold is minimized at the wavelength corresponding to the A-exciton resonant. At the resonance wavelength, the saturation threshold in both WS<sub>2</sub> and WSe<sub>2</sub> escalates with an increase in the number of layers. The analytical solution to the dynamics equation reveals the ultrafast dynamics of exciton density under different pulse durations. It implies that the choice of pulse duration plays a crucial role in observing the saturation threshold and the nonlinearity of the material. Specifically, longer pulse durations are beneficial for significantly large single pulse energy, while shorter pulses are more effective in reaching the threshold intensity if the single pulse energy is limited. Our results contribute valuable insights into the design of TMD-based active optical devices and highlight the importance of laser parameters when exploring the  $\chi^{(3)}$  nonlinearity of optical materials.

**Funding.** Key R&D Program of Hubei (2022BAA016); National Natural Science Foundation of China (12134011).

**Disclosures.** The authors declare no conflicts of interest.

**Data availability.** Data underlying the results presented in this paper are not publicly available at this time but may be obtained from the authors upon reasonable request.

**Supplemental document.** See [Supplement 1](#) for supporting content.

#### References

1. S. Z. Butler, S. M. Hollen, L. Cao, *et al.*, "Progress, challenges, and opportunities in two-dimensional materials beyond graphene," *ACS Nano* **7**(4), 2898–2926 (2013).
2. A. K. Geim and K. S. Novoselov, "The rise of graphene," *Nat. Mater.* **6**(3), 183–191 (2007).
3. B. Munkhbat, B. Küçüköz, D. G. Baranov, *et al.*, "Nanostructured transition metal dichalcogenide multilayers for advanced nanophotonics," *Laser Photonics Rev.* **17**(1), 2200057 (2023).
4. Q. H. Wang, K. Kalantar-Zadeh, A. Kis, *et al.*, "Electronics and optoelectronics of two-dimensional transition metal dichalcogenides," *Nat. Nanotechnol.* **7**(11), 699–712 (2012).
5. J. R. Schaibley, H. Yu, G. Clark, *et al.*, "Valleytronics in 2D materials," *Nat. Rev. Mater.* **1**(11), 16055–15 (2016).
6. T. Fryett, A. Zhan, and A. Majumdar, "Cavity nonlinear optics with layered materials," *Nanophotonics* **7**(2), 355–370 (2017).
7. Q. Bao, H. Zhang, Y. Wang, *et al.*, "Atomic-layer graphene as a saturable absorber for ultrafast pulsed lasers," *Adv. Funct. Mater.* **19**(19), 3077–3083 (2009).
8. Q. Bao, H. Zhang, Z. Ni, *et al.*, "Monolayer graphene as a saturable absorber in a mode-locked laser," *Nano Res.* **4**(3), 297–307 (2011).
9. D. Popa, Z. Sun, F. Torrisi, *et al.*, "Sub 200 fs pulse generation from a graphene mode-locked fiber laser," *Appl. Phys. Lett.* **97**(20), 203106 (2010).

10. J. Sotor, I. Pasternak, A. Krajewska, *et al.*, "Sub-90 fs a stretched-pulse mode-locked fiber laser based on a graphene saturable absorber," *Opt. Express* **23**(21), 27503–27508 (2015).
11. Z. Sun, T. Hasan, F. Torrisi, *et al.*, "Graphene mode-locked ultrafast laser," *ACS Nano* **4**(2), 803–810 (2010).
12. Z. Sun, D. Popa, T. Hasan, *et al.*, "A stable, wideband tunable, near transform-limited, graphene-mode-locked, ultrafast laser," *Nano Res.* **3**(9), 653–660 (2010).
13. Q. Bao, H. Zhang, J. x. Yang, *et al.*, "Graphene–polymer nanofiber membrane for ultrafast photonics," *Adv. Funct. Mater.* **20**(5), 782–791 (2010).
14. H. Zhang, Q. Bao, D. Tang, *et al.*, "Large energy soliton erbium-doped fiber laser with a graphene-polymer composite mode locker," *Appl. Phys. Lett.* **95**(14), 141103 (2009).
15. E. J. Lee, S. Y. Choi, H. Jeong, *et al.*, "Active control of all-fibre graphene devices with electrical gating," *Nat. Commun.* **6**(1), 6851 (2015).
16. O. Kovalchuk, S. Uddin, S. Lee, *et al.*, "Graphene capacitor-based electrical switching of mode-locking in all-fiberized femtosecond lasers," *ACS Appl. Mater. Interfaces* **12**(48), 54005–54011 (2020).
17. K. Chen, X. Zhou, X. Cheng, *et al.*, "Graphene photonic crystal fibre with strong and tunable light–matter interaction," *Nat. Photonics* **13**(11), 754–759 (2019).
18. R. I. Woodward and E. J. Kelleher, "2D saturable absorbers for fibre lasers," *Appl. Sci.* **5**(4), 1440–1456 (2015).
19. C. Ma, C. Wang, B. Gao, *et al.*, "Recent progress in ultrafast lasers based on 2D materials as a saturable absorber," *Appl. Phys. Rev.* **6**(4), 041304 (2019).
20. K. Wang, J. Wang, J. Fan, *et al.*, "Ultrafast saturable absorption of two-dimensional MoS<sub>2</sub> nanosheets," *ACS Nano* **7**(10), 9260–9267 (2013).
21. S. Bikorimana, P. Lama, A. Walser, *et al.*, "Nonlinear optical responses in two-dimensional transition metal dichalcogenide multilayer: WS<sub>2</sub>, WSe<sub>2</sub>, MoS<sub>2</sub> and Mo<sub>0.5</sub>W<sub>0.5</sub>S<sub>2</sub>," *Opt. Express* **24**(18), 20685–20695 (2016).
22. Y. Li, N. Dong, S. Zhang, *et al.*, "Giant two-photon absorption in monolayer MoS<sub>2</sub>," *Laser Photonics Rev.* **9**(4), 427–434 (2015).
23. R. Woodward, R. Howe, T. Runcorn, *et al.*, "Wideband saturable absorption in few-layer molybdenum diselenide (MoSe<sub>2</sub>) for Q-switching Yb-, Er-and Tm-doped fiber lasers," *Opt. Express* **23**(15), 20051–20061 (2015).
24. S. Zhang, N. Dong, N. McEvoy, *et al.*, "Direct observation of degenerate two-photon absorption and its saturation in WS<sub>2</sub> and MoS<sub>2</sub> monolayer and few-layer films," *ACS Nano* **9**(7), 7142–7150 (2015).
25. B. Chen, X. Zhang, K. Wu, *et al.*, "Q-switched fiber laser based on transition metal dichalcogenides MoS<sub>2</sub>, MoSe<sub>2</sub>, WS<sub>2</sub>, and WSe<sub>2</sub>," *Opt. Express* **23**(20), 26723–26737 (2015).
26. K. Wang, Y. Feng, C. Chang, *et al.*, "Broadband ultrafast nonlinear absorption and nonlinear refraction of layered molybdenum dichalcogenide semiconductors," *Nanoscale* **6**(18), 10530–10535 (2014).
27. G. Wang, G. Liang, A. A. Baker-Murray, *et al.*, "Nonlinear optical performance of few-layer molybdenum diselenide as a slow-saturable absorber," *Photonics Res.* **6**(7), 674–680 (2018).
28. K. Wu, X. Zhang, J. Wang, *et al.*, "WS<sub>2</sub> as a saturable absorber for ultrafast photonic applications of mode-locked and Q-switched lasers," *Opt. Express* **23**(9), 11453–11461 (2015).
29. M. Zhang, G. Hu, G. Hu, *et al.*, "Yb- and Er-doped fiber laser Q-switched with an optically uniform, broadband WS<sub>2</sub> saturable absorber," *Sci. Rep.* **5**(1), 17482 (2015).
30. K. Surbhi, S. Bhakta, A. Kumari, *et al.*, "Impact of pauli-blocking effect on optical limiting properties of WSe<sub>2</sub> thin films," *Opt. Mater.* **129**, 112479 (2022).
31. M. Khanzadeh and S. Marashi, "Laser beam intensity and wavelength dependent nonlinear absorption in pulse laser deposited WS<sub>2</sub> thin films," *Opt. Mater.* **127**, 112249 (2022).
32. T. Zhang and J. Wang, "Defect-enhanced exciton–exciton annihilation in monolayer transition metal dichalcogenides at high exciton densities," *ACS Photonics* **8**(9), 2770–2780 (2021).
33. C. Lu, M. Luo, Y. Ge, *et al.*, "Layer-dependent nonlinear optical properties of WS<sub>2</sub>, MoS<sub>2</sub>, and Bi<sub>2</sub>S<sub>3</sub> films synthesized by chemical vapor deposition," *ACS Appl. Mater. Interfaces* **14**(1), 2390–2400 (2022).
34. A. Chernikov, C. Ruppert, H. M. Hill, *et al.*, "Population inversion and giant bandgap renormalization in atomically thin WS<sub>2</sub> layers," *Nat. Photonics* **9**(7), 466–470 (2015).
35. C. Ruppert, A. Chernikov, H. M. Hill, *et al.*, "The role of electronic and phononic excitation in the optical response of monolayer WS<sub>2</sub> after ultrafast excitation," *Nano Lett.* **17**(2), 644–651 (2017).
36. C. Trovatiello, F. Katsch, Q. Li, *et al.*, "Disentangling many-body effects in the coherent optical response of 2D semiconductors," *Nano Lett.* **22**(13), 5322–5329 (2022).
37. H. Wang, C. Zhang, and F. Rana, "Ultrafast dynamics of defect-assisted electron–hole recombination in monolayer MoS<sub>2</sub>," *Nano Lett.* **15**(1), 339–345 (2015).
38. D. Erkensten, S. Brem, and E. Malic, "Exciton-exciton interaction in transition metal dichalcogenide monolayers and van der Waals heterostructures," *Phys. Rev. B* **103**(4), 045426 (2021).
39. E. A. Pogna, M. Marsili, D. De Fazio, *et al.*, "Photo-induced bandgap renormalization governs the ultrafast response of single-layer MoS<sub>2</sub>," *ACS Nano* **10**(1), 1182–1188 (2016).
40. R. Schmidt, G. Berghäuser, R. Schneider, *et al.*, "Ultrafast coulomb-induced intervalley coupling in atomically thin WS<sub>2</sub>," *Nano Lett.* **16**(5), 2945–2950 (2016).
41. F. Katsch, M. Selig, and A. Knorr, "Exciton-scattering-induced dephasing in two-dimensional semiconductors," *Phys. Rev. Lett.* **124**(25), 257402 (2020).

42. A. Kavokin, T. C. H. Liew, C. Schneider, *et al.*, “Polariton condensates for classical and quantum computing,” *Nat. Rev. Phys.* **4**(7), 435–451 (2022).
43. G. Muñoz-Matutano, A. Wood, M. Johnsson, *et al.*, “Emergence of quantum correlations from interacting fibre-cavity polaritons,” *Nat. Mater.* **18**(3), 213–218 (2019).
44. J. Yin, J. Li, H. Chen, *et al.*, “Large-area highly crystalline WSe<sub>2</sub> atomic layers for ultrafast pulsed lasers,” *Opt. Express* **25**(24), 30020–30031 (2017).
45. K. S. Novoselov, A. K. Geim, S. V. Morozov, *et al.*, “Electric field effect in atomically thin carbon films,” *Science* **306**(5696), 666–669 (2004).
46. K. Choi, Y. T. Lee, S.-W. Min, *et al.*, “Direct imprinting of MoS<sub>2</sub> flakes on a patterned gate for nanosheet transistors,” *J. Mater. Chem. C* **1**(47), 7803–7807 (2013).
47. H. Zeng, G.-B. Liu, J. Dai, *et al.*, “Optical signature of symmetry variations and spin-valley coupling in atomically thin tungsten dichalcogenides,” *Sci. Rep.* **3**(1), 1608 (2013).
48. W. Zhao, Z. Ghorannevis, L. Chu, *et al.*, “Evolution of electronic structure in atomically thin sheets of WS<sub>2</sub> and WSe<sub>2</sub>,” *ACS Nano* **7**(1), 791–797 (2013).
49. Y. Li and T. F. Heinz, “Two-dimensional models for the optical response of thin films,” *2D Mater.* **5**(2), 025021 (2018).
50. Q. Hao, K. Ye, M. Dong, *et al.*, “Nonlinear optical response of a monolayer WS<sub>2</sub> and the application of a hundred-MHz nanosecond laser,” *Opt. Express* **29**(22), 36634–36643 (2021).
51. Y. Yu, Y. Yu, C. Xu, *et al.*, “Fundamental limits of exciton-exciton annihilation for light emission in transition metal dichalcogenide monolayers,” *Phys. Rev. B* **93**(20), 201111 (2016).
52. L. Yuan and L. Huang, “Exciton dynamics and annihilation in WS<sub>2</sub> 2D semiconductors,” *Nanoscale* **7**(16), 7402–7408 (2015).